A hydrodynamic analysis of self-similar radiative ablation flows. Supplementary material

J. - M. Clarisse[1]†, J. - L. Pfister[2], S. Gauthier[3] and C. Boudesocque-Dubois[1]

[1]CEA, DAM, DIF, Bruyères-le-Châtel, F-91297 Arpajon, France

[2]Present address: ONERA-The French Aerospace Lab, 8, rue des Vertugadins, F-92190 Meudon, France

[3]Present address: ChebyPhys, F-26100 Romans-sur-Isère, France

(Received 18 April 2018)

Appendix A. Analytical approximations of self-similar solutions

Solutions computed in §3 with the numerical method of Boudesocque-Dubois *et al.* (2013) may be compared with approximate analytical solutions derived under particular assumptions.

A.1. *Shock wave approximation*

Upon considering the reduced system of equations (3.5) in the absence of heat conduction, analytical approximations of self-similar shock waves for boundary pressures (3.7a) can be obtained under the form of perturbation expansions. In the case of the $(\mathcal{B}_p, \mathcal{B}_\varphi)$-formulation (§2.2.1), these expansions yield, at leading order, the approximations

$$\mathcal{S}_G(\tilde{\xi}) = G_{\mathsf{d}} \left[\eta \frac{\mathcal{B}_p}{\xi_{\rm sf}^2} - \left(\eta \frac{\mathcal{B}_p}{\xi_{\rm sf}^2} - 1 \right) \tilde{\xi} \right]^{1/\gamma} \tilde{\xi}^{-b}, \tag{A 1a}$$

$$\mathcal{S}_V(\tilde{\xi}) = V_{\mathsf{d}} \left[1 + \frac{\gamma-1}{2}\, \eta^{-1/\gamma} \left(\frac{b}{b+1} \big(1 - \tilde{\xi}^{b+1}\big) + \frac{1}{\gamma}\, \frac{\eta-1}{\eta}\, \frac{b+1}{b+2} \big(1 - \tilde{\xi}^{b+2}\big) \right) \right], \tag{A 1b}$$

$$\mathcal{S}_\Theta(\tilde{\xi}) = \Theta_{\mathsf{d}} \left[\eta \frac{\mathcal{B}_p}{\xi_{\rm sf}^2} - \left(\eta \frac{\mathcal{B}_p}{\xi_{\rm sf}^2} - 1 \right) \tilde{\xi} \right]^{(\gamma-1)/\gamma} \tilde{\xi}^{b}, \tag{A 1c}$$

valid for $0 < \tilde{\xi} \leqslant 1$, where $\tilde{\xi} = \xi/\xi_{\rm sf}$, $b = 2(\alpha-1)/\alpha\gamma$, $\eta = (\gamma+1)/2\alpha^2$, and G_{d}, V_{d}, Θ_{d} are the downstream shock front values (3.8). A rather good agreement, for such approximations at leading order, with computed solutions at small heat fluxes is found over the flow compressed regions: see figure 14.

† Email address for correspondence: jean-marie.clarisse@cea.fr

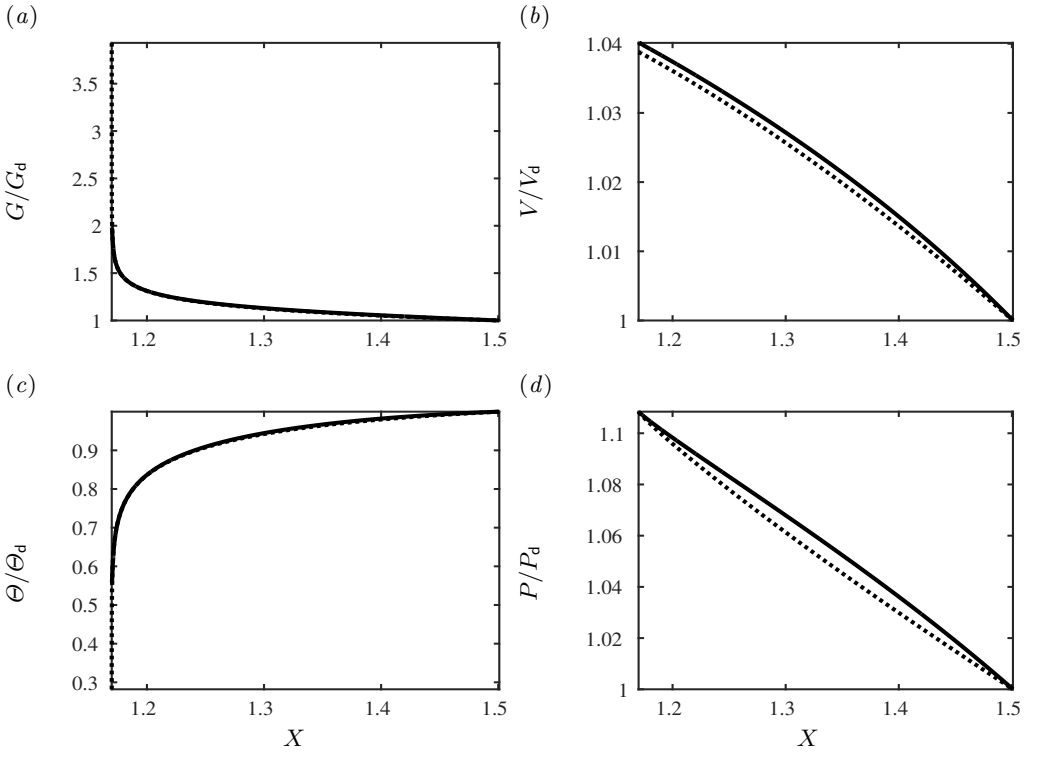

FIGURE 14. Comparion of the shock wave approximations (⋯), given by (A 1), with the vanishing conduction region flow (—) of figure 5 (profiles with the smallest spatial extent). Spatial profiles in the reduced coordinate X of the flow reduced (a) density, (b) velocity, (c) temperature, and (d) pressure, normalized by their downstream shock front values.

A.2. *Conduction region approximation*

Perturbation expansions of the solutions to the full system of reduced equations (3.5), for $\mu = 2$, with boundary conditions (3.7) give the leading order approximations

$$\mathcal{C}_G(\tilde{\xi}) = G(0)\left(1-\tilde{\xi}\right)^{-1/(\nu+2)}, \tag{A 2a}$$

$$\mathcal{C}_V(\tilde{\xi}) = V(0) + \frac{\alpha\,\xi_a}{G(0)}\,\frac{\nu+2}{\nu+3}\left[1-\left(1+\frac{\tilde{\xi}}{\nu+2}\right)\left(1-\tilde{\xi}\right)^{1/(\nu+2)}\right], \tag{A 2b}$$

$$\mathcal{C}_\Theta(\tilde{\xi}) = \Theta(0)\left(1-\tilde{\xi}\right)^{1/(\nu+2)}, \tag{A 2c}$$

valid for $0 \leqslant \tilde{\xi} < 1$, with $\tilde{\xi} = \xi/\xi_a$ and $\xi_a = \mathcal{B}_p^{-1}\mathcal{B}_\varphi^{-1}\Theta(0)^{\nu+2}/(\nu+2)$. This latter parameter which corresponds to a singularity of the density function (A 2a) and a zero of the temperature function (A 2c), can be considered as the approximate location of the ablation front. These approximate solutions result from a uniform pressure approximation of the flow conduction regions and are best verified for flows presenting expansion waves with significant quasi-isobaric portions (figure 15).

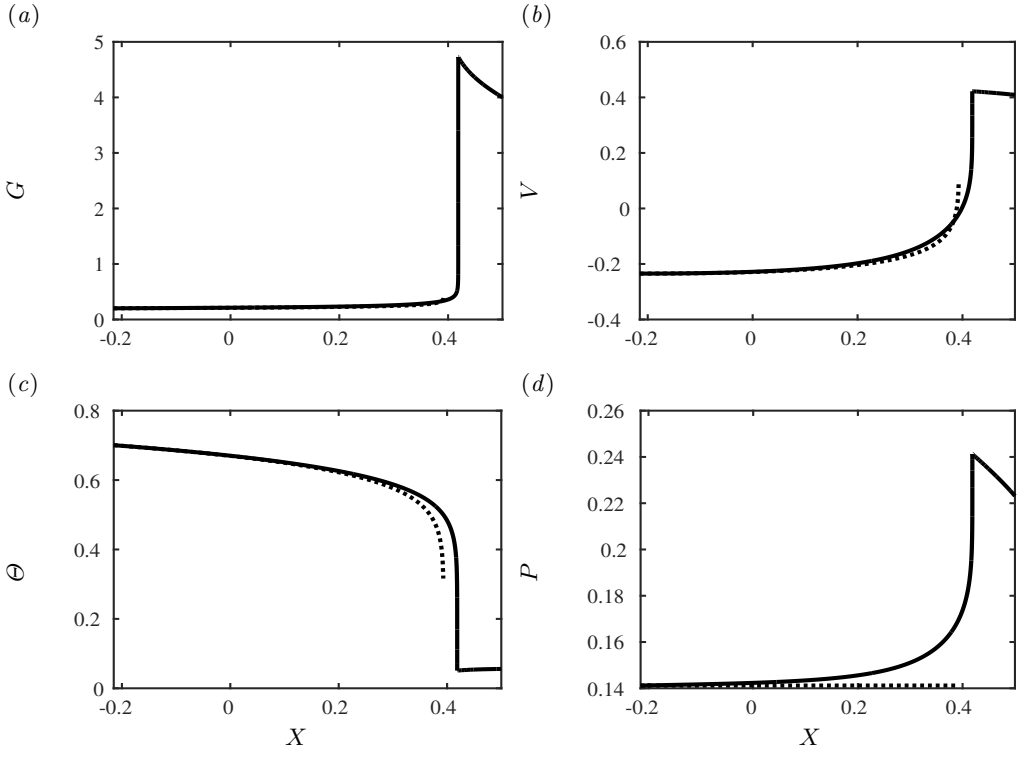

FIGURE 15. Comparion of the conduction region approximations (⋯) deduced from (A 2) with a stiff ablation flow (—) presenting a nearly isobaric portion of its conduction region. Spatial profiles in the reduced coordinate X of the flow reduced (a) density, (b) velocity, (c) temperature, and (d) pressure, normalized by their downstream shock front values.

Appendix B. Quantitative hydrodynamic analysis

B.1. *Ablative wave spatial structure*

Solutions of the chart $(\mathcal{B}_\varphi, \mathcal{B}_p)$ may display spatial variations of very different steepness as illustrated in figures 5–7, by profiles of the flow-variable reduced functions vs the reduced coordinate X for some of the flows identified in the chart of figure 3. Such profiles are homothetic to the actual profiles in physical space (coordinate x) of the flow physical variables: reduced abscissas and ordinates only need to be multiplied by the products of the proper variable scale of table 1(a) and the relevant power of t given by (3.2) and table 7.

All of the flow solutions are characterized by density and velocity absolute maxima as well as a temperature absolute minimum located in the upstream vicinity of the ablation front. (Here and throughout the rest of the paper, upstream and downstream are defined relatively to the flow passing through the leading shock-wave front.) The accelerated shock wave is sustained by a compression wave extending downstream to the shock front all the way to the density maximum, i.e. spanning almost entirely the compressed fluid region, with characteristic profiles of increasing density, velocity and pressure across the wave (figures 5–7a, b, d). Temperature (figures 5–7c) and entropy (figures 16–18b) are however decreasing across this wave as a consequence of the increasing production of entropy at the accelerating shock front and diffusion of heat from the shock front towards the ablation front (see figures 16–18a in which cusps, characterizing vanishing heat flux values, mark the boundaries between left regions of inward, $\varphi_x > 0$, and right regions of

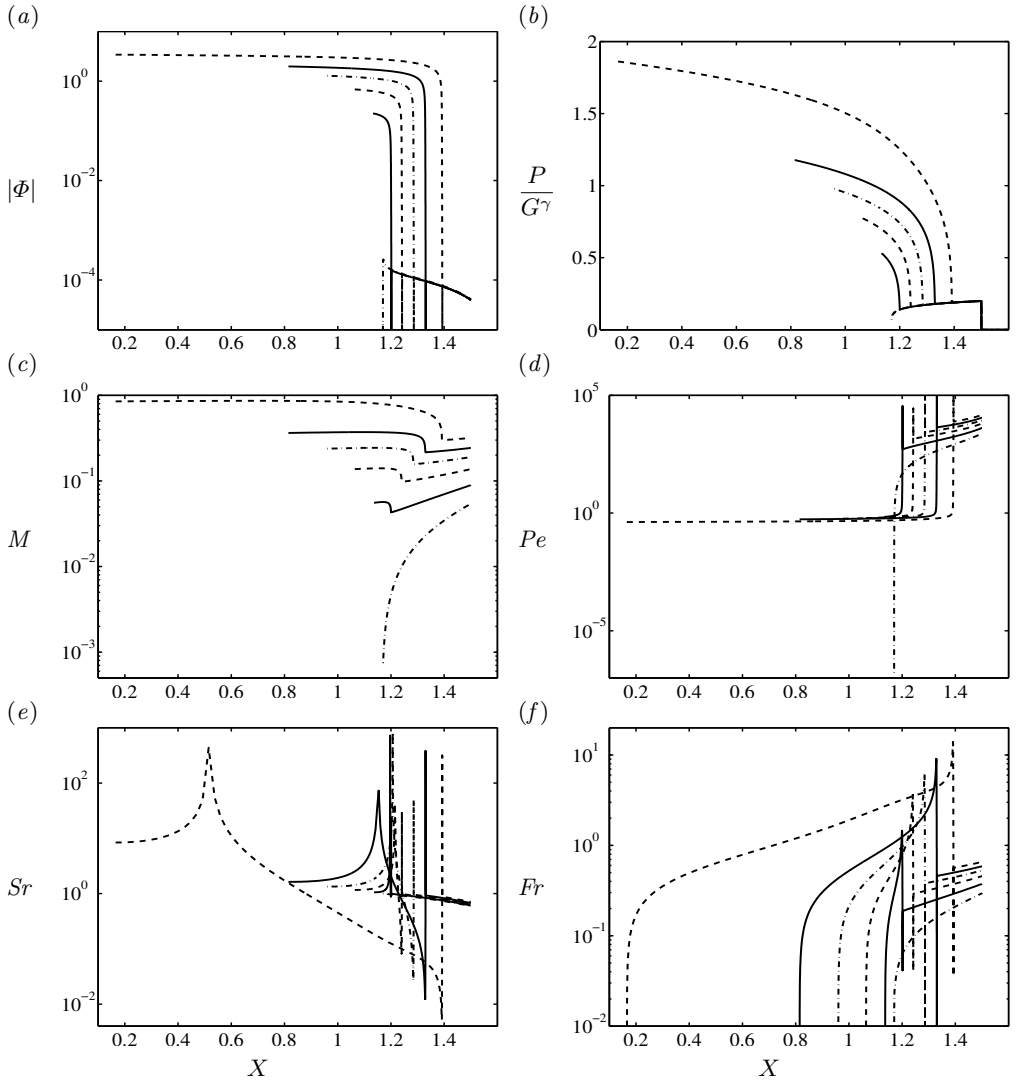

FIGURE 16. Reduced function profiles in the reduced coordinate X of solutions obtained with the $(\mathcal{B}_p, \mathcal{B}_\varphi)$-formulation — solution sample $\xi_{\rm sf} = 1.5$ (symbols $*$ in figure 3). Flow (a) reduced absolute heat flux $|\Phi|$, (b) reduced specific-entropy exponential P/G^γ (see table 7), (c) Mach number $M\big(V', C_s\big)$, (d) Péclet number $Pe\big(V', L_{\nabla T}, G^{-\mu-1}\,\Theta^\nu\big)$, (e) stratification number $Sr\big(L_{\nabla p}, \mathcal{H}(C_T, A_{\rm af})\big)$, (f) and Froude number $Fr\big(V', L_{\nabla v'_x}, A_{\rm af}\big)$. Corresponding profiles of the flow reduced density, velocity, temperature and pressure are given in figure 5.

outward, $\varphi_x < 0$, diffusion of heat). In the conduction region, the temperature (figures 5–7c) and heat flux (see figures 16–18a) are both increasing whereas the density and velocity (figures 5–7a, b) decrease as the distance to the external boundary diminishes. Quite differently, depending on the external boundary pressure level, pressure profiles may either be increasing (cf. the flow with $X_{\rm sf} = 2$ in figure 6d), either comprise a maximum in the upstream vicinity of the ablation front followed by a minimum further downstream (cf. the flows with $X_{\rm sf} \leqslant 1.5$ in figure 6d), either exhibit a single maximum upstream to the front (case of figure 7d). In all the cases, the heated fluid expansion is neither isothermal (figures 5–7c) nor isentropic (figures 16–18b).

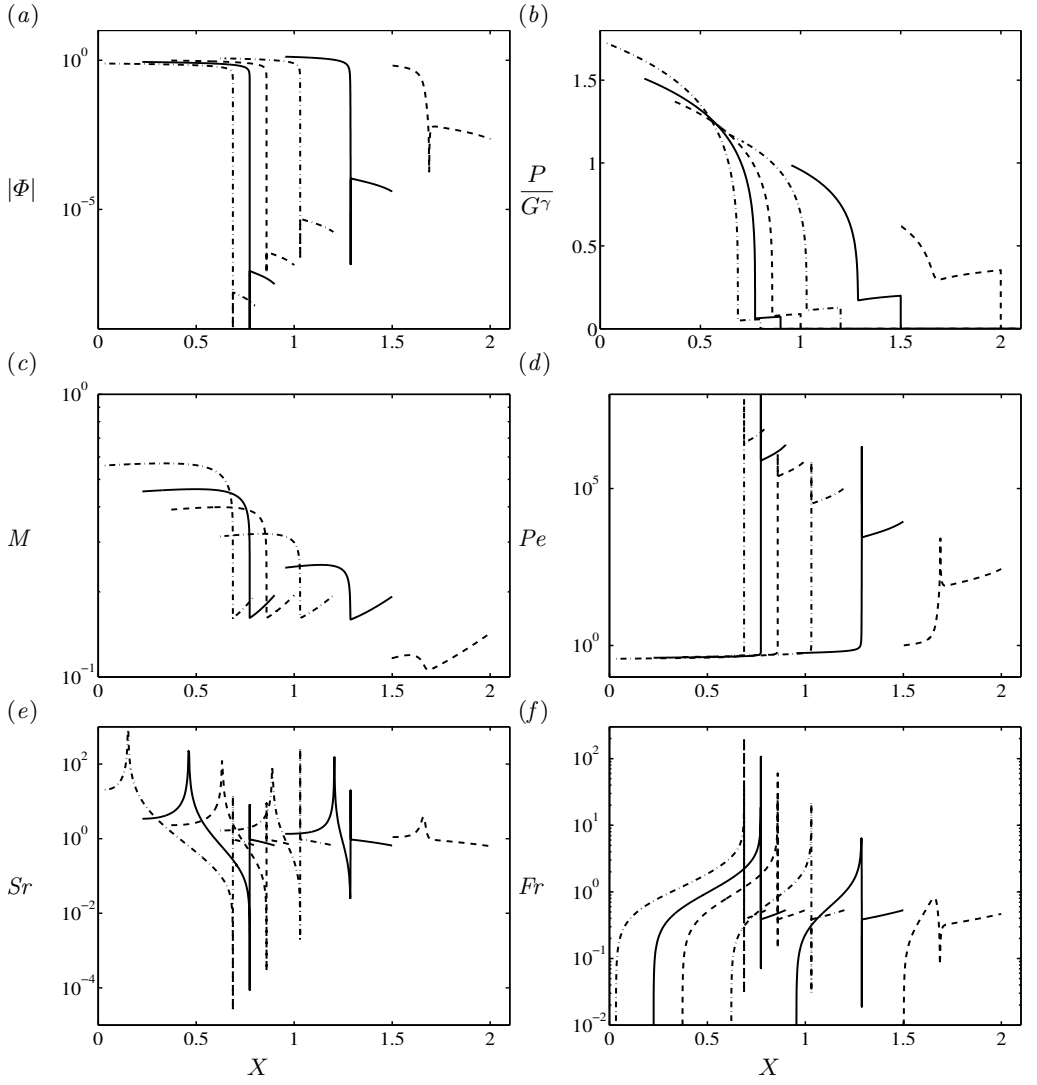

FIGURE 17. Reduced function profiles in the reduced coordinate X of solutions obtained with the $(\mathcal{B}_p, \mathcal{B}_\varphi)$-formulation — solution sample $\xi_f/\xi_{\rm sf} = 0.4$ (symbols ○ in figure 3). Conventions identical to those of figure 16. Corresponding profiles of the flow reduced density, velocity, temperature and pressure are given in figure 6.

This wide variety of flow profiles is quantitatively transcribed into the values of the relative characteristic lengths of the conduction region, $L_{\rm cond}/L_{\rm tot}$ (figures 19*a*, *b*), and of the ablation front, $L_T/L_{\rm tot}$ (figures 19*c*, *d*). The former appears to be essentially — flows with vanishing conduction regions being set aside — an increasing function of the Péclet scale $\mathcal{P}e$ (figure 19*b*), or equivalently of the ratio $\mathcal{B}_\varphi/\mathcal{B}_p$ (cf. table 2), ranging from 0% to over 90%. Hence the extent and, consequently, the expansion of the conduction region are mainly controlled by the relative magnitude of the external boundary heat flux with respect to the external boundary pressure. Flows with the largest conduction regions are found in the region of heat-conduction dominated flows as defined by criterion $v_{\rm pw}(t)/v_{\rm tw}(t) < 1$ with (3.11): cf. figure 4. These characteristic features — extent and expansion — of the conduction region, and therefore of the complementary

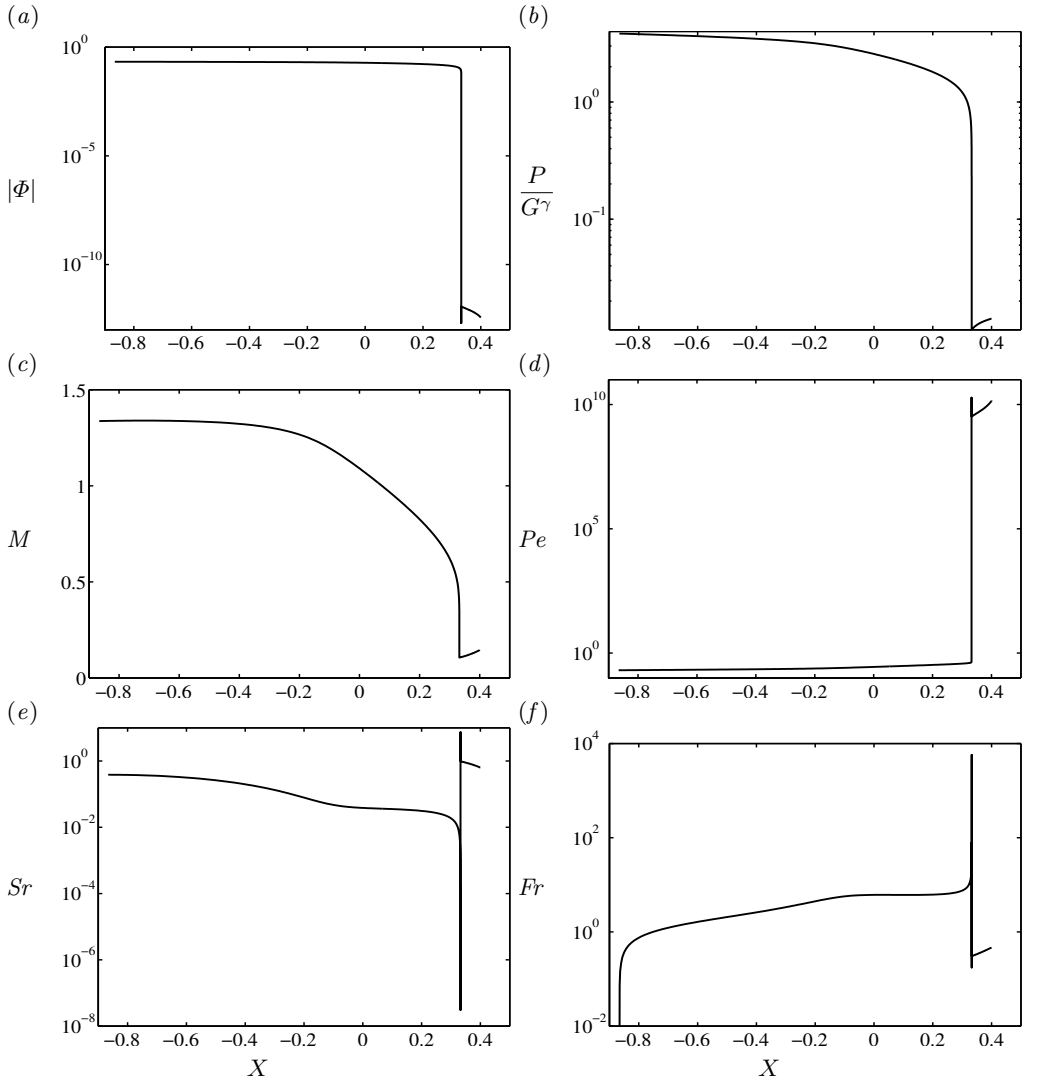

FIGURE 18. Reduced function profiles in the reduced coordinate X of solutions obtained with the $(\mathcal{B}_p, \mathcal{B}_\varphi)$-formulation — IPI-like solution (symbol □ in figure 3). Conventions identical to those of figure 16. Corresponding profiles of the flow reduced density, velocity, temperature and pressure are given in figure 7.

compressed fluid region, are ruling parameters of the transmission of flow perturbations between the external surface, the ablation layer and the leading shock-wave front. As such, their role are influential in the dynamics of the flow perturbations, especially at large perturbation (relative) wavelengths (e.g. see Goncharov *et al.* 2000; Clarisse *et al.* 2016).

The ablation-front scale length, L_T, is another determining parameter of the flow hydrodynamic stability properties. Corresponding to the smallest diffusion length-scale of the flow, L_T is indicative of the perturbation wavelength below which any perturbation within the conduction region and the ablation layer would be, in principle, smoothed out, thus determining a wavelength lower bound of the flow-perturbation amplification spectrum. The relative magnitude of the ablation-front scale length, $L_T/L_{\rm tot}$, measuring

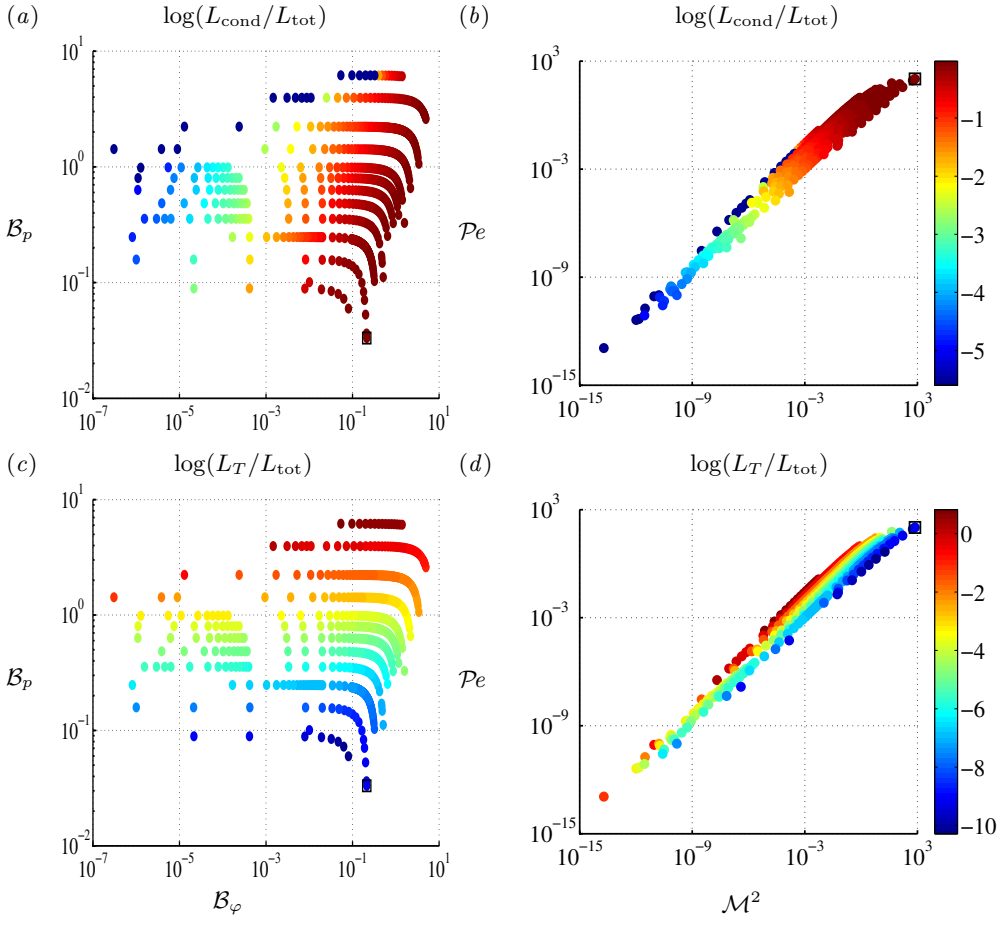

FIGURE 19. Conduction-zone relative length $L_{\rm cond}/L_{\rm tot}$ and flow stiffness $L_T/L_{\rm tot}$ for the solutions of figures 3, 4. Solutions are represented by a colored dot (IPI-like solution $\square$) in both (*a*, *c*) the plane $(\mathcal{B}_\varphi, \mathcal{B}_p)$ and (*b*, *d*) the plane $(\mathcal{M}^2, \mathcal{P}e)$, according to the color scales given by the full ranges, in logarithmic scales, of: (*a*, *b*) the conduction-zone relative length, $0 \leqslant L_{\rm cond}/L_{\rm tot} \leqslant 0.96$; (*c*, *d*) the flow stiffness, $5\,10^{-11} \leqslant L_T/L_{\rm tot} \leqslant 6.6$.

the *ablation front stiffness*, evolves as a function, mainly, of the ratio $\mathcal{P}e/\mathcal{M}^2 \propto \mathcal{B}_p$ (figure 19*d*) and, moderately, of the boundary heat flux parameter $\mathcal{B}_\varphi$ (figure 19*c*). Flows with the highest ablation front stiffnesses ($L_T/L_{\rm tot}$ as low as 10^{-10}) correspond to the smallest boundary pressures that have been handled so far with the present numerical method of solution, and comprise the IPI-like flow solution. Assessing the hydrodynamic stability of such flows would imply sampling the perturbation wavelength spectrum over many decades. These high stiffness values are a consequence of the radiation heat conduction approximation of radiation transport. Less simplistic treatments of actual radiative ablation would lead, for comparable boundary pressure and radiative flux levels, to lower stiffnesses. At the other end of the ablation-front stiffness range ($L_T/L_{\rm tot} \gtrsim 1$) are flows driven by the highest dimensionless boundary pressures $\mathcal{B}_p$ (figures 19*c*, *d*). For such flows, perturbation damping by heat-conduction is expected to be effective up to large (relative) values of the perturbation wavelength.

B.2. *Hydrodynamic characteristic numbers*

The analysis of the hydrodynamic properties of the present ablative flows relies on the equations of motion (2.1) written in the reference frame of the ablation front with the help of the Cartesian coordinate x, viz

$$\frac{\mathrm{D}\rho}{\mathrm{D}t} + \rho\,\frac{\partial v'_x}{\partial x} = 0, \tag{B 1a}$$

$$\rho\,\frac{\mathrm{D}v'_x}{\mathrm{D}t} + \frac{\partial p}{\partial x} + \rho\,a_{\mathrm{af}} = 0, \tag{B 1b}$$

$$\rho\,\frac{\mathrm{D}}{\mathrm{D}t}\left(\frac{1}{2}{v'_x}^2 + \mathrm{C}_v T\right) + \frac{\partial}{\partial x}(p v'_x + \varphi_x) + \rho\,a_{\mathrm{af}}\,v'_x = 0, \tag{B 1c}$$

with the notation

$$\frac{\mathrm{D}.}{\mathrm{D}t} = \frac{\partial.}{\partial t} + v'_x\,\frac{\partial.}{\partial x}, \tag{B 2}$$

for the material derivative, $v'_x(x,t) = v_x(x,t) - \mathrm{d}x_{\mathrm{af}}(t)/\mathrm{d}t$ for the fluid velocity relative to the front, and a_{af} for the front acceleration.

The local properties of the flows are then assessed by comparing, at any given flow location:

- Inertia forces with pressure forces in (B 1*b*), through the ratio

$$\left|\frac{\rho\,v'_x\,\partial v'_x/\partial x}{\partial p/\partial x}\right| = \gamma\,M^2(v'_x, c_s), \tag{B 3}$$

where $M(v'_x, c_s)$ is the isentropic Mach number with respect to the ablation front (cf. table 8*a* for notations)

- The work of pressure forces, $p\,v'_x$, with the heat flux, φ_x, in the energy equation (B 1*c*), by means of the ratio

$$\left|\frac{p\,v'_x}{\varphi_x}\right| = \frac{\ell_{\nabla T}\,|v'_x|}{\kappa/\rho\,R} = Pe(v'_x, \ell_{\nabla T}, \kappa/\rho\,R), \tag{B 4}$$

thus defining a Péclet number based on the local temperature-gradient length $\ell_{\nabla T}$.

- Pressure forces vs acceleration forces in the momentum equation (B 1*b*), through the ratio

$$\left|\frac{1}{\rho\,a_{\mathrm{af}}}\,\frac{\partial p}{\partial x}\right| = \left\{\ell_{\nabla p}/\big(p/\rho\,|a_{\mathrm{af}}|\big)\right\}^{-1} = \frac{1}{Sr\big(\ell_{\nabla p}, \mathcal{H}(c_T, a_{\mathrm{af}})\big)}, \tag{B 5}$$

which amounts to the inverse of a stratification number, Sr, defined in terms of the local pressure-gradient length $\ell_{\nabla p}$.

- Convective vs acceleration effects in (B 1*b*), through the ratio

$$\left|\frac{1}{a_{\mathrm{af}}}\,v'_x\,\frac{\partial v'_x}{\partial x}\right| = Fr^2(v'_x, \ell_{\nabla v'_x}, a_{\mathrm{af}}), \tag{B 6}$$

which defines a Froude number based on the local velocity-gradient length $\ell_{\nabla v'_x}$.

Such definitions of Péclet, stratification and Froude numbers which rely on distinct local gradient lengths (table 8), are required for accurately rendering the flow actual properties. Analysis of these numbers for the present set of ablative flows (§3) has been conducted within the two classifications of self-similar solutions provided by the charts $(\mathcal{B}_\varphi, \mathcal{B}_p)$ and $(\mathcal{M}, \mathcal{P}e)$ with the help of the corresponding reduced expressions (table 8*b*): cf. figures 20–23. General features common to all flows, flow region specific properties as well as an identification of the hydrodynamic regimes that the present ablative waves may belong to, come out from this analysis.

(a)

Number	Mach	Péclet	Stratification	Froude
Function	$M(v,c)=\dfrac{\lvert v\rvert}{c}$	$Pe(v,\ell,\chi)=\dfrac{\ell\,\lvert v\rvert}{\chi}$	$Sr(\ell,H)=\dfrac{\ell}{H}$, with $\mathcal{H}(c,g)=\dfrac{c^2}{\lvert g\rvert}$	$Fr(v,\ell,g)=\dfrac{\lvert v\rvert}{\sqrt{\lvert g\rvert\,\ell}}$

(b)

Number	Type of analysis	Definition	Reduced expression
Mach	local/LM	$M(v'_x,c_s)$	$M(V',C_s)$
Péclet	local	$Pe(v'_x,\ell_{\nabla T},\kappa/\rho\,R)$	$Pe\big(V',L_{\nabla T},G^{-\mu-1}\,\Theta^{\nu}\big)$
	LM	$Pe(v'_x,\ell_{\nabla T},\kappa/\mathrm{C}_p\,\rho)$	$Pe\big(V',L_{\nabla T},(\gamma-1)G^{-\mu-1}\,\Theta^{\nu}/\gamma\big)$
Stratification	local	$Sr\big(\ell_{\nabla p},\mathcal{H}(c_T,a_{\mathrm{af}})\big)$	$Sr\big(L_{\nabla p},\mathcal{H}(C_T,A_{\mathrm{af}})\big)$
	LM	$Sr\big(\ell_{\nabla v'_x},\mathcal{H}(c_T,a_{\mathrm{af}})\big)$	$Sr\big(L_{\nabla v'_x},\mathcal{H}(C_T,A_{\mathrm{af}})\big)$
Froude	local/LM	$Fr(v'_x,\ell_{\nabla v'_x},a_{\mathrm{af}})$	$Fr\big(V',L_{\nabla v'_x},A_{\mathrm{af}}\big)$

TABLE 8. (a) Function notations and (b) definitions of hydrodynamic characteristic numbers used for the local flow analysis (§B.2) and LM-approximation analysis (§B.3) with corresponding reduced expressions for the self-similar solutions of §3 in the $(\mathcal{B}_p,\mathcal{B}_\varphi)$-formulation (§2.2.1). Additional notations and definitions are those of table 7.

Values of the Mach number $M(V',C_s)$ are characterized by an absolute minimum reached in the vicinity of the ablation front and local maxima at the shock front and within the conduction region (figures 16–18c). For all flows, singular values of the Péclet number $Pe\big(V',L_{\nabla T},G^{-\mu-1}\,\Theta^{\nu}\big)$ arise at the temperature minimum coinciding with the upstream edge of the ablation layer (figures 16–18d). Singular values of the stratification number $Sr\big(L_{\nabla p},\mathcal{H}(C_T,A_{\mathrm{af}})\big)$ also occur for flows with vanishing pressure gradients (figures 16–18e), possibly inducing extreme variations of this number in the ablation layer and further downstream. The Froude number $Fr\big(V',L_{\nabla v'_x},A_{\mathrm{af}}\big)$ spans its full range across the expansion wave, from $Fr=0$ — at both the fluid external boundary and the fluid-velocity maximum upstream to the ablation front — to its maximum reached about the ablation front (figures 16–18f).

Conduction region. As expected in a region where heat conduction is important, values of the Péclet number are smaller than one, confirming the dominance "diffusion > convection". However this dominance is limited since $Pe>0.3$ for the vast majority of the sampled flows (figure 20a, b) — exceptions made of flows with vanishing heat conduction regions for which $Pe\to 0$ — indicating that the work of pressure forces cannot be neglected in front of the energy flux. The expansion flow of the heated fluid ranges from being entirely subsonic (figures 16, 17c) to being partially supersonic (figure 18c). The latter case corresponds to ablative waves with the highest Mach values (figures 21a, b) which are such that $\mathcal{P}e>10^2$ (figure 21b) and which are identified as being dominantly driven by heat conduction, according to the criterion $v_{\mathrm{pw}}(t)/v_{\mathrm{tw}}(t)<1$ given by (3.11): cf. figure 4. Such ablative waves present an isentropic Chapman–Jouguet (CJ) point in their conduction region — i.e. $M\big(V',C_s\big)(\xi_{\mathrm{cj}})=1$, $0<\xi_{\mathrm{cj}}<\xi_{\mathrm{af}}$ — delimitating a subregion $0\leqslant\xi<\xi_{\mathrm{cj}}$ where acoustic waves cannot propagate towards the ablation front. The actual subregion of supersonic expansion extends in fact further upstream to this CJ point since the speed of pressure waves is smaller than the isentropic sound velocity in this part of the

flow. Ablative waves presenting isentropic CJ points include the IPI-like flow of figure 3 (figures 21*a*, *b*) and flows with vanishing external boundary pressures (e.g. Saillard *et al.* 2010) which are relevant to ICF. The balance between acceleration and pressure forces — stratification number (figures 16–18*e*) — on one hand, and between convection and acceleration effects — Froude number (figures 16–18*f*) — on the other hand, may vary significantly across the region, pointing out the actual hydrodynamic heterogeneity of the heated fluid flow. This heterogeneity is especially pronounced, regarding the former, for flows presenting a pressure minimum within the conduction region (values of Sr above ten in figures 22*a*, *b*) for which Sr may range from $Sr \ll 1$ (figures 22*c*, *d*) to $Sr \gg 1$, and, with respect to the latter, for flows with $\max_\xi Fr \gg 1$ (figures 17, 18*f*, and 23*a*, *b*).

Ablation layer. The ablation layer, being the boundary between regions of high (downstream) and low (upstream) heat conduction, is primarily characterized by the trans-critical transition of the Péclet number (figures 16–18*d*). With $Pe|_{\xi_{\mathrm{af}}} \approx 4.$ at the ablation front (figures 20*c*, *d*) — except for vanishing conduction-region flows for which $Pe|_{\xi_{\mathrm{af}}} \to 0$ — pressure-force work slightly and constantly dominates heat diffusion in the front immediate vicinity. Non-negligible compressible effects in the layer — and therefore throughout the whole ablative waves — are to be expected for flows with the highest values of $\mathcal{B}_\varphi$ as $\gamma M^2(V', C_s)|_{\xi_{\mathrm{af}}}$ takes values in excess of 1/10 up to 1/4 and above (figure 21*c*). Very subsonic ablation velocities are obtained for solutions with small values of the Péclet scale $\mathcal{P}e$ (figure 21*d*) or, almost equivalently, characterized by small extents of their conduction regions (figure 19*b*). These solutions agree with the criterion of hydrodynamically dominated flows $v_{\mathrm{pw}}(t)/v_{\mathrm{tw}}(t) > 1$ defined by (3.11): see figure 4. Ablative waves with sufficiently low (high) values of $\mathcal{M}$ have acceleration effects dominating (respectively, being dominated by) both pressure gradients — $Sr > 1$ (figures 22*e*, *f*) — and convection — $Fr < 1$ (figures 23*c*, *d*) — in a neighbourhood of their ablation front. However, the coexistence of local velocity and temperature — plus, eventually, pressure — extrema, on the upstream side of the layer, with the steepest gradients of velocity, temperature — respectively, pressure — about the ablation front, induce extreme spatial variations of the Péclet (figures 16–18*d*) and Froude numbers (figures 16–18*f*) — respectively, stratification number (figures 16–18*e*) — across the layer. Consequently, apart from acceleration-dominated flows — i.e. such that $\max_\xi Fr < 1$ (figures 23*a*, *b*) — for which the ordering "acceleration > convection" prevails, no clear-cut hierarchy of physical effects can be drawn over the ablation layer as a whole.

Compressed fluid region. In terms of hydrodynamic characteristic numbers, the compressed fluid region, away from the ablation layer, consistently appears to be rather homogeneous in space (figures 16–18). Mach number values if remaining subsonic, vary significantly (over nearly a decade, cf. figure 16*c*) as the whole set of flows is spanned. Values of the Péclet number, while staying characteristic of a low heat conduction, span an extremely large range as $\mathcal{B}_p$ is varied (figures 16*f* and 20*e*, *f*). On the contrary and quite remarkably, the stratification and Froude numbers remain consistently within the same limited ranges (figures 16–18*e*, *f*), $0.5 \leqslant Sr \leqslant 2$ and $0.1 < Fr < 0.72$, evidencing that, within the compressed region, pressure and acceleration effects are comparable and prevail over convective effects. The hierarchy of physical effects remains thus the same, namely "pressure ≈ acceleration > convection > diffusion".

Examination of the overall properties exhibited by the self-similar solutions of §3, leads to the identification of some particular flow regimes that are summarized in table 4:

(i) Ablative waves with supersonic fluid velocities, i.e. such that $\max M(V', C_s) > 1$ or, equivalently, presenting an isentropic Chapman–Jouguet point. Corresponding to a supersonic expansion of part of their conduction region, these flows lie in the

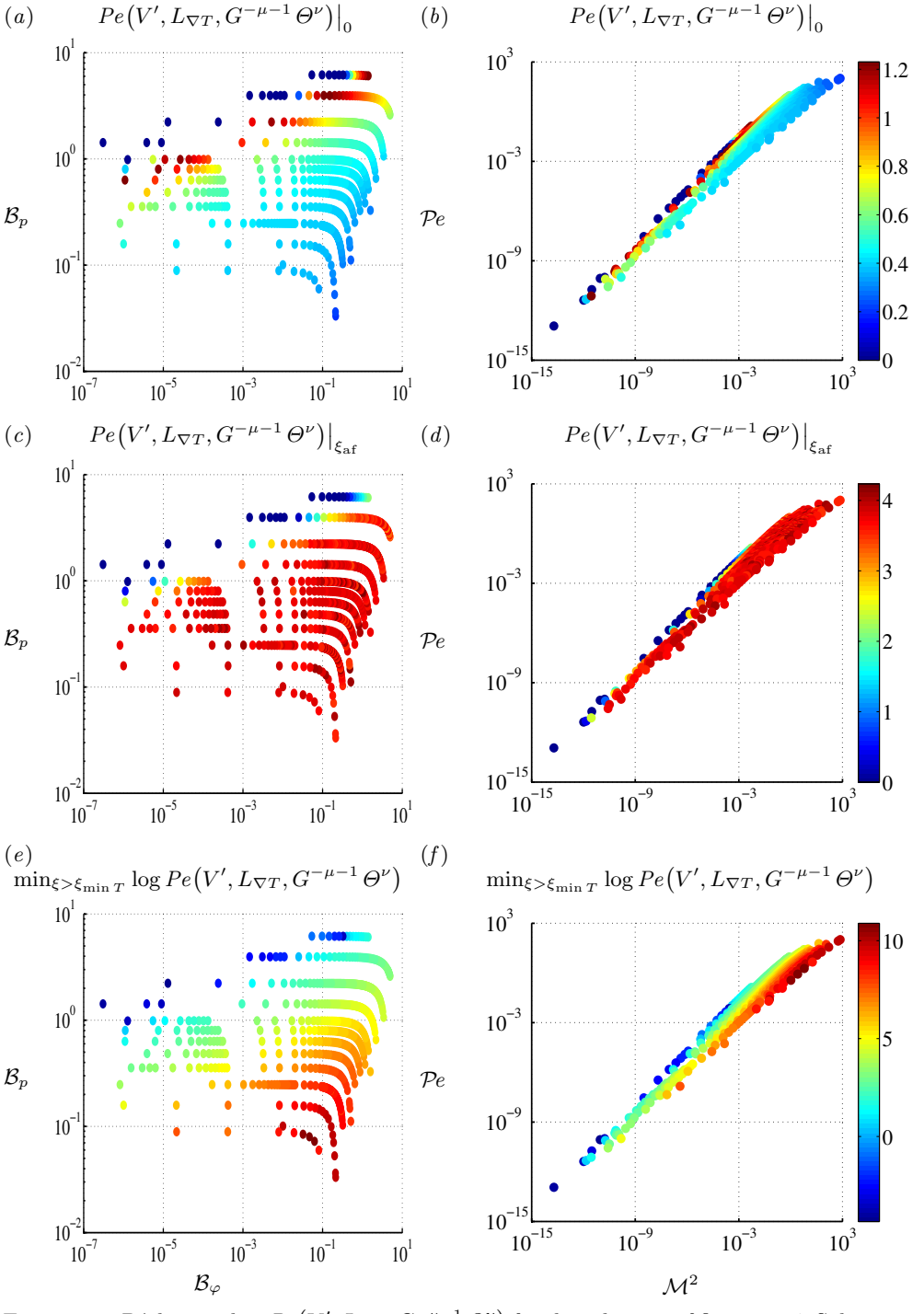

FIGURE 20. Péclet number $Pe\big(V', L_{\nabla T}, G^{-\mu-1}\,\Theta^{\nu}\big)$ for the solutions of figures 3, 4. Solutions are represented by a colored dot in both (*a*, *c*, *e*) the plane $(\mathcal{B}_\varphi, \mathcal{B}_p)$ and (*b*, *d*, *f*) the plane $(\mathcal{M}^2, \mathcal{P}e)$, according to the color scales given by the full ranges of: (*a*, *b*) the conduction-region minimum value, $0 \leqslant Pe\big(V', L_{\nabla T}, G^{-\mu-1}\,\Theta^{\nu}\big)|_0 \leqslant 1.23$; (*c*, *d*) the ablation-front value, $0 \leqslant Pe\big(V', L_{\nabla T}, G^{-\mu-1}\,\Theta^{\nu}\big)|_{\xi_{\rm af}} \leqslant 4.23$; (*e*, *f*) the logarithm of the minimum value over the low-heat-diffusion region, $1.8\,10^{-5} \leqslant \min_{\xi>\xi_{\min T}} Pe\big(V', L_{\nabla T}, G^{-\mu-1}\,\Theta^{\nu}\big) \leqslant 4.8\,10^{10}$.

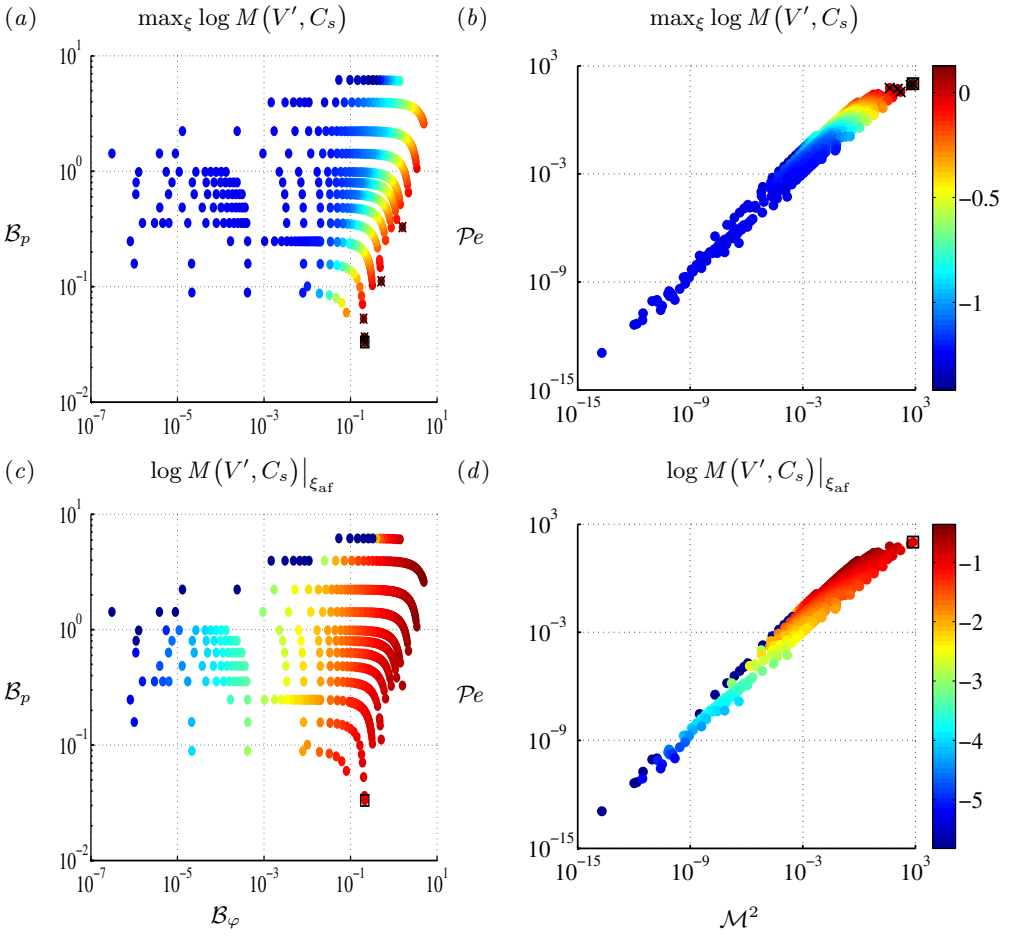

FIGURE 21. Mach number $M(V', C_s)$ for the solutions of figures 3, 4. Solutions are represented by a colored dot (IPI-like solution □) in both (*a*, *c*) the plane $(\mathcal{B}_\varphi, \mathcal{B}_p)$ and (*b*, *d*) the plane $(\mathcal{M}^2, \mathcal{P}e)$, according to the color scales given by the full ranges, in logarithmic scales, of: (*a*, *b*) the overall flow maximum value, $0.038 \leqslant \max_\xi M(V', C_s) \leqslant 1.34$; (*c*, *d*) the ablation front value, $0 < M(V', C_s)|_{\xi_{\rm af}} \leqslant 0.44$. Flows with an isentropic Chapman–Jouguet point, i.e. for which $\max_\xi M(V', C_s) \geqslant 1$, are also indicated (×) in (*a*, *b*).

region $\mathcal{P}e > 10^2$ of the plane $(\mathcal{M}^2, \mathcal{P}e)$ (see figure 21*b*) and are, according to the criterion $v_{\rm pw}(t)/v_{\rm tw}(t) < 1$ with (3.11), dominated by heat conduction: cf. figures 3 and 4.

(ii) Ablative waves with sufficiently high ablation velocities, so that compressible effects within the ablation layer, and therefore throughout the flow, are non-negligible, i.e. for which $\gamma M^2(V', C_s) > 0.1$. Such flows, identified by $M(V', C_s)|_{\xi_{\rm af}} > 0.24$ in figures 21(*c*, *d*), are obtained for the highest values of the external radiative heat flux.

(iii) Ablative waves for which acceleration dominates convection, i.e. such that $Fr(V', L_{\nabla v'_x}, A^{\rm e}_{\rm af}) < 1$. Obtained for boundary pressures sufficiently high with respect to the external radiative heat fluxes, in effect for $\mathcal{B}_p > 4.0\,\mathcal{B}_\varphi^{0.29}$, these flows lie in the region $v_{\rm pw}(t)/v_{\rm tw}(t) > 1$, with (3.11), and are, accordingly, mainly driven by hydrodynamic effects. Pressure forces may locally dominate acceleration forces in such flows but not to the point of the latters being negligible: $Sr\big(L_{\nabla p}, \mathcal{H}(C_T, A^{\rm e}_{\rm af})\big) > 0.1$ (figure 22*c*, *d*).

(iv) Ablative waves in which the flow through the ablation front sees convection

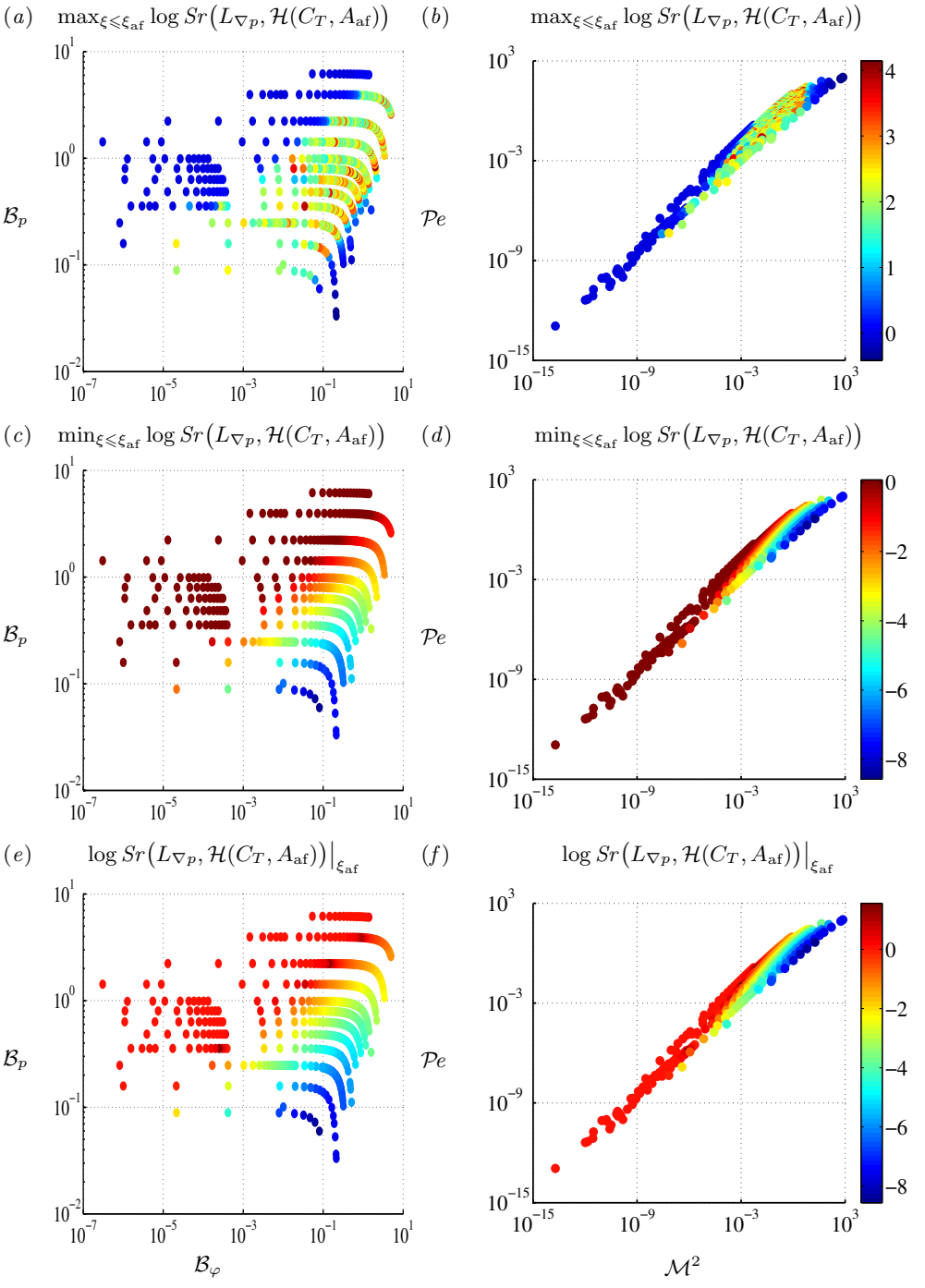

FIGURE 22. Stratification number $Sr\big(L_{\nabla p},\mathcal{H}(C_T,A_{\rm af})\big)$ for the solutions of figures 3, 4. Solutions are represented by a colored dot in both (*a*, *c*, *e*) the plane $(\mathcal{B}_\varphi,\mathcal{B}_p)$ and (*b*, *d*, *f*) the plane $(\mathcal{M}^2,\mathcal{P}e)$, according to the color scales given by the full ranges, in logarithmic scales, of: (*a*, *b*) the conduction region maximum value, $0.4 \leqslant \max_{\xi\leqslant\xi_{\rm af}} Sr\big(L_{\nabla p},\mathcal{H}(C_T,A_{\rm af})\big) \leqslant 1.4\,10^4$; (*c*, *d*) the conduction region minimum value, $2.6\,10^{-9} \leqslant \min_{\xi\leqslant\xi_{\rm af}} Sr\big(L_{\nabla p},\mathcal{H}(C_T,A_{\rm af})\big) \leqslant 1.2$; (*e*, *f*) the ablation-front value, $2.7\,10^{-9} \leqslant Sr\big(L_{\nabla p},\mathcal{H}(C_T,A_{\rm af})\big)|_{\xi_{\rm af}} \leqslant 36$.

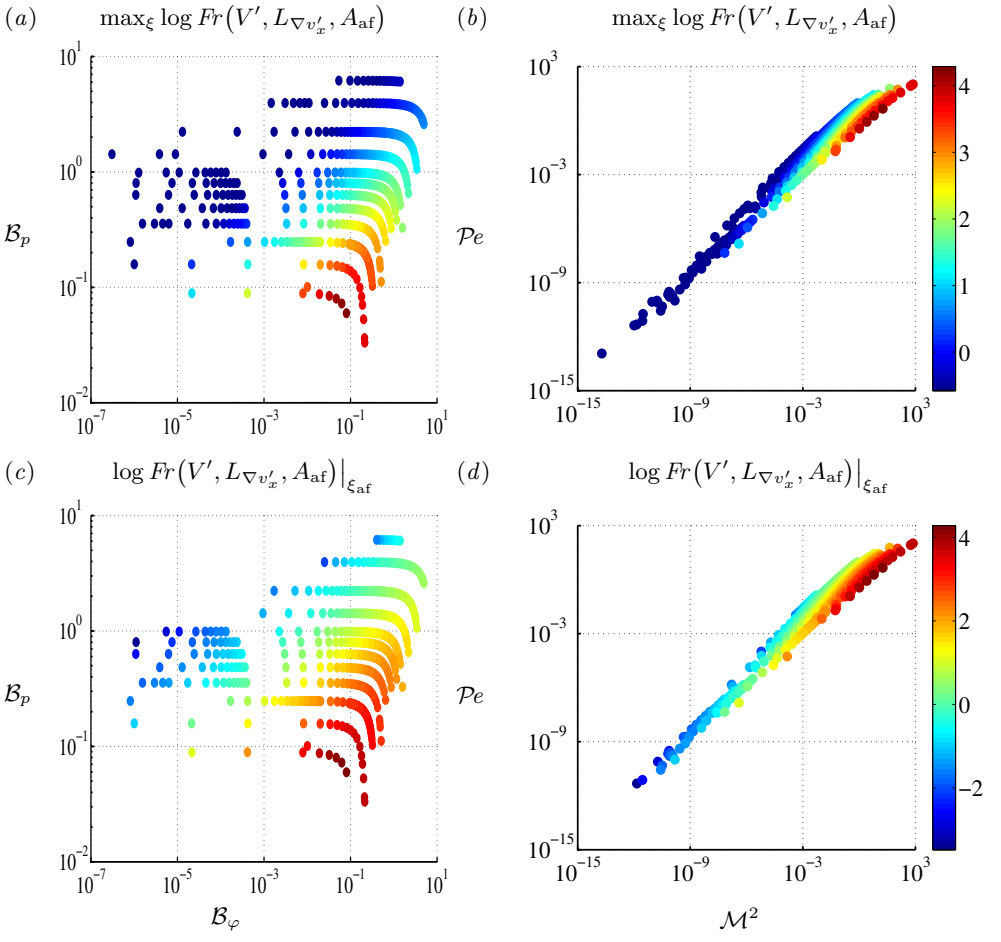

FIGURE 23. Froude number $Fr(V', L_{\nabla v'_x}, A_{\rm af})$ for the solutions of figures 3, 4. Solutions are represented by a colored dot in both (*a*, *c*) the plane $(\mathcal{B}_\varphi, \mathcal{B}_p)$ and (*b*, *d*) the plane $(\mathcal{M}^2, \mathcal{P}e)$, according to the color scales given by the full ranges, in logarithmic scales, of: (*a*, *b*) the overall flow maximum value, $0.26 \leqslant \max_\xi Fr(V', L_{\nabla v'_x}, A_{\rm af}) \leqslant 1.9\,10^4$; (*c*, *d*) the ablation-front value, $3.3\,10^{-4} \leqslant Fr(V', L_{\nabla v'_x}, A_{\rm af})|_{\xi_{\rm af}} \leqslant 1.9\,10^4$.

effects dominating acceleration effects, i.e. with $Fr(V', L_{\nabla v'_x}, A^{\rm e}_{\rm af})|_{\xi_{\rm af}} > 1$. Observed for irradiations that are sufficiently intense compared to the external boundary pressures, i.e. for $3.7\,\mathcal{B}_\varphi^{0.3} > \mathcal{B}_p$, the corresponding flows include the fast expansion and fast ablation flow regimes identified in items (i) and (ii) above.

B.3. *Low-Mach-number analysis*

The subsonic character of ablation fronts in ICF has been used in numerous instances whether for the sole purpose of modelling ablative flows (e.g. see, for laser-driven ablation, the review of Bychkov *et al.*, 2015, and, for x-ray driven ablation, Nozaki & Nishihara, 1980; Saillard *et al.*, 2010), whether with the goal of obtaining simplified mean-flow equations for a hydrodynamic stability analysis (cf. Bychkov *et al.* 2015, and references therein). Among the latters, a significant number of hydrodynamic stability studies have relied on the 'isobaric' model of laser ablation introduced in ICF by Kull & Anisimov (1986). This isobaric model is in fact nothing else but an application, to laser ablation, of

the 'low Mach number (LM) approximation' originally developed for problems of natural convection (Paolucci 1982). The widespread use of this model in ICF and its potential application to hydrodynamic stability analyses of x-ray ablation, call for its evaluation on the present set of self-similar solutions held as realistic examples of radiative ablation flows. The foregoing analysis ressembles that perfomed in (Boudesocque-Dubois *et al.* 2008) for self-similar flows with electron heat conduction $(\mu,\nu) = (0, 5/2)$ and related to laser-driven ablation, but differs in the actual definitions of the LM approximation criteria.

B.3.1. *Criteria of the low-Mach-number approximation*

The present analysis of the LM approximation for a general ablation flow relies on the (M', Fr', Pe')-formulation of the equations of motion (§2.2.3) written for the ablation-front reference frame but in Eulerian form with the help of the dimensionless cartesian coordinate $\bar{x}$. The energy equation being reformulated as in (Paolucci 1982), the corresponding form of (2.25) ensues as

$$\frac{\mathrm{D}\bar{\rho}}{\mathrm{D}\bar{t}} + \bar{\rho}\,\frac{\partial \bar{v}'_x}{\partial \bar{x}} = 0, \tag{B 7a}$$

$$\bar{\rho}\,\frac{\mathrm{D}\bar{v}'_x}{\mathrm{D}\bar{t}} + \frac{1}{\gamma\, M'^2}\,\frac{\partial \bar{p}}{\partial \bar{x}} + \frac{\bar{\rho}}{Fr'^2} = 0, \tag{B 7b}$$

$$\bar{\rho}\,\frac{\mathrm{D}\bar{T}}{\mathrm{D}\bar{t}} - \frac{\gamma-1}{\gamma}\,\frac{\mathrm{D}\bar{p}}{\mathrm{D}\bar{t}} + \frac{1}{Pe'}\,\frac{\partial \bar{\varphi}_x}{\partial \bar{x}} = 0, \tag{B 7c}$$

with: the relevant variant of (B 2) for the material derivative; expressions (2.17), (2.18); and (2.26) where we have chosen $a_c^{\mathsf{e}} = a_{\mathrm{af}}$ for the acceleration reference value of table 1(*c.ii*). Choosing the remaining reference values, ρ_c, T_c, v'_c, to be — at first — the corresponding flow values at the ablation front and $\ell_c = \ell_T$, the LM approximation of (B 7) considers expansions of the form (Paolucci 1982)

$$\bar{q} = \bar{q}^{(0)} + \gamma\, M'^2\, \bar{q}^{(1)} + o\big(\gamma\, M'^2\big), \tag{B 8}$$

for any fluid variable q, assuming that

$$\gamma\, M'^2 \ll 1. \tag{B 9}$$

Inserting such expansions into (B 7) yields:

- at the lowest order in $\gamma\, M'^2$, the equation

$$\frac{\partial \bar{p}^{(0)}}{\partial \bar{x}} = 0, \tag{B 10}$$

as obtained from (B 7b), provided that

$$\gamma\, M'^2/Fr'^2 \ll 1\,; \tag{B 11}$$

- at the following order in $\gamma\, M'^2$, the system

$$\frac{\mathrm{D}\bar{\rho}^{(0)}}{\mathrm{D}\bar{t}} + \bar{\rho}^{(0)}\,\frac{\partial \bar{v}'^{(0)}_x}{\partial \bar{x}} = 0, \tag{B 12a}$$

$$\bar{\rho}^{(0)}\,\frac{\mathrm{D}\bar{v}'^{(0)}_x}{\mathrm{D}\bar{t}} + \frac{1}{\gamma\, M'^2}\,\frac{\partial \bar{p}^{(1)}}{\partial \bar{x}} + \frac{\bar{\rho}^{(0)}}{Fr'^2} = 0, \tag{B 12b}$$

$$\bar{\rho}^{(0)}\,\frac{\mathrm{D}\bar{T}^{(0)}}{\mathrm{D}\bar{t}} - \frac{\gamma-1}{\gamma}\,\frac{\mathrm{d}\bar{p}^{(0)}}{\mathrm{d}\bar{t}} + \frac{1}{Pe'}\,\frac{\partial \bar{\varphi}^{(0)}_x}{\partial \bar{x}} = 0, \tag{B 12c}$$

along with $\bar{p}^{(0)} = \bar{\rho}^{(0)}\,\bar{T}^{(0)}$, $\bar{\varphi}^{(0)}_x = -\big(\bar{\rho}^{(0)}\big)^{-\mu}\,\big(\bar{T}^{(0)}\big)^{\nu}\,\partial \bar{T}^{(0)}/\partial \bar{x}$, as deduced from (B 7)

under the condition that, in the expansion of (B 7c), the term in $\gamma\, M'^2/Pe'$ is of the same order as $\gamma\, M'^2$, i.e.

$$\gamma\, M'^2/Pe' \ll 1\,. \tag{B 13}$$

The LM approximation (B 10), (B 12) is thus bound to the fulfillment of the three requirements — or *LM-approximation criteria* — (B 9), (B 11), (B 13): cf. Paolucci (1982). The isobaric model of Kull & Anisimov (1986) corresponds to the steady flow instance of (B 10), (B 12), yet without the framework of the expansions (B 8). In particular, the Péclet number criterion (B 13) is absent from the paper of Kull & Anisimov (1986) and consequently from all the ensuing works relying on this model (e.g. see Bychkov *et al.* 1994; Goncharov *et al.* 1996; Clavin & Masse 2004).

For strongly spatially inhomogeneous flows such as some of the ablative waves of §3, the validity of the LM approximation (B 10), (B 12) must be established over a neighbourhood of the ablation front, say $\mathcal{V}$, rather than merely at the front itself. The resulting criteria replacing (B 9), (B 11), (B 13) come then as, with the notations of table 8,

$$\gamma\, M^2(v'_x, c_s) \ll 1, \tag{B 14a}$$

$$\frac{\gamma\, M^2(v'_x, c_s)}{Fr^2(v'_x, \ell_{\nabla v'_x}, a_{\rm af})} = Sr\big(\ell_{\nabla v'_x}, \mathcal{H}(c_T, a_{\rm af})\big) \ll 1, \tag{B 14b}$$

$$\frac{\gamma\, M^2(v'_x, c_s)}{Pe(v'_x, \ell_{\nabla T}, \kappa/\mathrm{C}_p\,\rho)} \ll 1, \tag{B 14c}$$

for any point of $\mathcal{V}$. These criteria follow from changing the reference values, ρ_c, T_c, v'_c, in (B 7) to be the flow values at a running point of $\mathcal{V}$, and for (B 14b), from the fact that (B 10) amounts to having $\partial\bar{p}/\partial\bar{x} = O\big(\gamma\, M^2(v'_x, c_s)\big)$ in (B 7b), while (B 14c) proceeds from noticing that (B 12c) requires that, in (B 7c), the heat flux term $(\partial\bar{\varphi}_x/\partial\bar{x})/Pe'$ is of the same order as the remaining terms. The above definition (B 14b) of the Froude criterion is identical to that given in (Kull & Anisimov 1986), but in many instances other reference lengths, in particular global lengths, have been used (e.g. Bychkov *et al.* 1994; Goncharov *et al.* 1996; Boudesocque-Dubois *et al.* 2008). In that respect, the above low-Mach-number analysis presents the advantage of leaving no ambiguity in the definitions of the required reference lengths.

B.3.2. *LM-approximation criteria verification*

The usefulness of a LM-approximation for the present set of self-similar ablation flows, is assessed by evaluating, for each flow, the sizes of the three neighbourhoods of the ablation front satisfying the following inequalities:

$$\gamma\, M^2(v'_x, c_s) \leqslant 0.1, \quad Sr\big(\ell_{\nabla v'_x}, \mathcal{H}(c_T, a_{\rm af})\big) \leqslant 0.1, \quad \frac{\gamma\, M^2(v'_x, c_s)}{Pe(v'_x, \ell_{\nabla T}, \kappa/\mathrm{C}_p\,\rho)} \leqslant 0.1\,. \tag{B 15a, b, c}$$

Away from the front, other flow regions may satisfy these inequalities but are discarded. The region of validity of the LM-approximation is then given by the intersection of these three neighbourhoods and is evaluated upon comparing the size of each neighbourhood with that of the ablation wave, $\ell_{\rm tot}$ (figure 24). None of the present ablative waves is suitable for a LM-approximation over its entire extent. Instead, flows belonging to the compressible regimes identified in §B.2 (cf. also table 4) either violate the small Mach-number criterion (B 15a) in the fast ablation case, either satisfy (B 15a) but over restricted portions, less than 20%, of their extent in the fast expansion case: see figures 24(a, b). Other flows, fulfilling criterion (B 15a) over larger extents ($\mathcal{M}^2 \lessapprox 1$ and $\mathcal{P}e \lessapprox 1$, in figure 24$b$), are constrained by the Froude number criterion (B 15b): ablation-

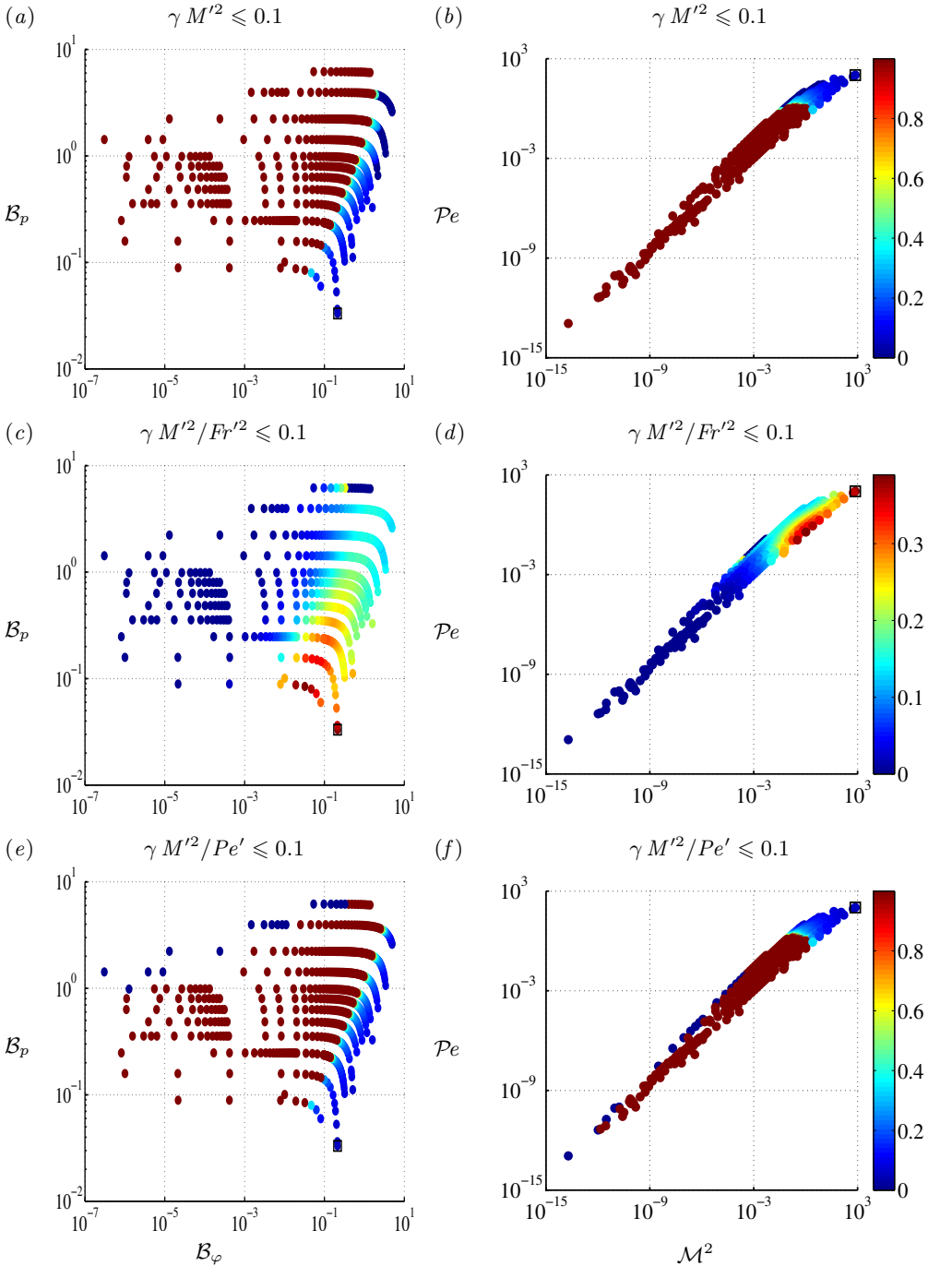

FIGURE 24. Extents of the LM-approximation validity regions for the solutions of figures 3, 4. Solutions are represented by a colored dot (IPI-like solution □) in both (*a*, *c*, *e*) the plane $(\mathcal{B}_\varphi, \mathcal{B}_p)$ and (*b*, *d*, *f*) the plane $(\mathcal{M}^2, \mathcal{P}e)$. The color scales are set by the full ranges of the relative sizes with respect to the ablation wave extent $\ell_{\rm tot}$, say $\ell_{\rm LM}/\ell_{\rm tot}$, of the ablation front neighbourhoods satisfying each of the three LM-approximation criteria (B 15), namely: (*a*, *b*) for the Mach number criterion (B 15*a*), $0 \leqslant \ell_{\rm LM}/\ell_{\rm tot} \leqslant 1$; (*c*, *d*) for the Froude number criterion (B 15*b*), $0 \leqslant \ell_{\rm LM}/\ell_{\rm tot} \leqslant 0.39$; (*e*, *f*) for the Péclet number criterion (B 15*c*), $0 \leqslant \ell_{\rm LM}/\ell_{\rm tot} \leqslant 1$. Actual inspection of the criteria (B 15) is performed on the solutions in the $(\mathcal{B}_p, \mathcal{B}_\varphi)$-formulation with the help of the reduced expressions deduced from table 7.

front neighbourhoods satisfying (B 15b) represent less than 40% of the ablative wave extent when they are not of vanishing sizes (figures 24c, d). In other words, regions of high flow stratifications are dominant: cf. figure 17(e). The Péclet number criterion (B 15c) follows roughly the Mach number criterion (compare figures 24a, b and e, f) and thus does not impose in most cases additional constraints, except for flows with vanishing conduction regions (figures 19a, b) for which the Péclet number becomes too small (cf. §B.2) for (B 15c) to be satisfied in the vicinity of the ablation front.

From these observations, a LM-approximation appears to be of little relevance for modelling flows taken from the present set of self-similar solutions. This conclusion may be extended to non self-similar ablation flows on the ground of hydrodynamic similitude. For example, a LM-approximation is obviously inappropriate for correctly describing the ablative flows with fast-expanding conduction regions, i.e. such that $\max M(v'_x, c_s) > 1$, that are characteristic (e.g. Saillard *et al.* 2010) of current ICF-pellet implosions driven by hohlraum-generated x-ray irradiation.

Appendix C. Eigenvalues and eigenvectors of the matrix $\boldsymbol{B}^0$

Eigenvalues, λ_k, $k = 1, 2, 3$, of the matrix $\boldsymbol{B}^0$ defined by (4.2b) are computed numerically using Cardano's formulas (e.g. see Jacobson 2009) for the roots of the cubic polynomial

$$P_3(\mu) = \mu^3 + p\,\mu + q, \tag{C 1}$$

with the expressions

$$\mu = \lambda - \frac{1}{3}\,q_T^0, \quad p = -\frac{1}{3}\,{q_T^0}^2 - \gamma\,{z_T^0}^2, \quad q = -\frac{2}{27}\,{q_T^0}^3 + \left[\left(1 - \frac{\gamma}{3}\right) q_T^0 - q_\rho^0\right] {z_T^0}^2, \tag{C 2}$$

λ being the eigenvalue unknown. The components l_i^k, $i = 1, 2, 3$, of the left eigenvector $\boldsymbol{l}^k$ associated to the eigenvalue λ_k are deduced from the relations

$$l_2^k = \frac{\rho^0 T^0}{{z_T^0}^2}\left(\lambda_k - q_T^0\right) l_3^k, \quad l_1^k = \frac{1}{{\rho^0}^2}\left[\lambda_k\, l_2^k - (\gamma - 1)\,\rho^0 T^0\, l_3^k\right], \tag{C 3}$$

where l_3^k may be freely specified, provided that it is non-zero, or determined from normalization arguments.

C.1. *Analytical approximations*

The expressions of the coefficients p and q in (C 2) allow for perturbation expansions of the analytical formulas for the roots of $P_3(\mu) = 0$ in terms of the quantities q_ρ^0/z_T^0 and q_T^0/z_T^0, or, alternatively, z_T^0/q_T^0, taken as small parameters. These expansions, carried out with Maxima (2010) under the assumption that the discriminant of $P_3(\mu)$ is negative, lead to the following results.

Case $|q_\rho^0| \ll z_T^0$ and $|q_T^0| \ll z_T^0$. Under the assumption $|q_\rho^0| \ll z_T^0$ and $|q_T^0| \ll z_T^0$, the following approximations for the eigenvalues of $\boldsymbol{B}^0$ are obtained

$$\left.\begin{aligned}
\lambda_1^{\mathrm{LH}} &= \sqrt{\gamma}\,z_T^0 + \frac{1}{2}\left[q_T^0 + \frac{1}{\gamma}\,(q_\rho^0 - q_T^0)\right] + O\Big(q_a^0\,q_b^0/{z_T^0}^2\Big),\\
\lambda_2^{\mathrm{LH}} &= \frac{1}{\gamma}\,(q_T^0 - q_\rho^0) + O\Big(q_a^0\,q_b^0\,q_c^0/{z_T^0}^3\Big),\\
\lambda_3^{\mathrm{LH}} &= -\sqrt{\gamma}\,z_T^0 + \frac{1}{2}\left[q_T^0 + \frac{1}{\gamma}\,(q_\rho^0 - q_T^0)\right] + O\Big(q_a^0\,q_b^0/{z_T^0}^2\Big),
\end{aligned}\right\} \tag{C 4}$$

where the subscripts a, b, c are any of ρ or T. The resulting approximations for the associated left eigenvectors, deduced from (C 3) with the choice $l^{\text{LH}\,k}_{\;\;3} = \rho^0$, come then as, respectively,

$$\left.\begin{aligned} l^{\text{LH}\,1}_{\;\;1} &= T^0 \left[1 + \frac{1}{\sqrt{\gamma}\, z_T^0}\,(q_\rho^0 - q_T^0) + O\Big(q_a^0\, q_b^0 / {z_T^0}^2\Big)\right], \\ l^{\text{LH}\,1}_{\;\;2} &= \gamma\, M'^2\, z_T^0 \left[\sqrt{\gamma} + \frac{1}{2\,\gamma\, z_T^0}\,\left[q_\rho^0 - (\gamma+1)\, q_T^0\right] + O\Big(q_a^0\, q_b^0 / {z_T^0}^2\Big)\right], \end{aligned}\right\} \tag{C 5a}$$

$$\left.\begin{aligned} l^{\text{LH}\,2}_{\;\;1} &= -(\gamma-1)\, T^0 + O\Big(q_a^0\, q_b^0 / {z_T^0}^2\Big), \\ l^{\text{LH}\,2}_{\;\;2} &= -M'^2\left[q_\rho^0 + (\gamma-1)\, q_T^0\right] + O\Big(q_a^0\, q_b^0 / {z_T^0}^2\Big), \end{aligned}\right\} \tag{C 5b}$$

$$\left.\begin{aligned} l^{\text{LH}\,3}_{\;\;1} &= T^0 \left[1 - \frac{1}{\sqrt{\gamma}\, z_T^0}\,(q_\rho^0 - q_T^0) + O\Big(q_a^0\, q_b^0 / {z_T^0}^2\Big)\right], \\ l^{\text{LH}\,3}_{\;\;2} &= \gamma\, M'^2\, z_T^0 \left[-\sqrt{\gamma} + \frac{1}{2\,\gamma\, z_T^0}\,\left[q_\rho^0 - (\gamma+1)\, q_T^0\right] + O\Big(q_a^0\, q_b^0 / {z_T^0}^2\Big)\right]. \end{aligned}\right\} \tag{C 5c}$$

Case $|q_T^0| \gg z_T^0$. When $|q_T^0| \gg z_T^0$, expansions of λ_k in terms of the parameter z_T^0/q_T^0 yield

$$\left.\begin{aligned} \lambda_1^{\text{HH}} &= q_T^0 + \left[q_\rho^0 + (\gamma-1)\, q_T^0\right] \frac{{z_T^0}^2}{{q_T^0}^2} + O\Big({z_T^0}^4 / {q_T^0}^4\Big), \\ \lambda_2^{\text{HH}} &= \sqrt{\left|1 - q_\rho^0/q_T^0\right|}\, z_T^0 - \frac{1}{2}\left[q_\rho^0 + (\gamma-1)\, q_T^0\right] \frac{{z_T^0}^2}{{q_T^0}^2} + O\Big({z_T^0}^3 / {q_T^0}^3\Big), \\ \lambda_3^{\text{HH}} &= -\sqrt{\left|1 - q_\rho^0/q_T^0\right|}\, z_T^0 - \frac{1}{2}\left[q_\rho^0 + (\gamma-1)\, q_T^0\right] \frac{{z_T^0}^2}{{q_T^0}^2} + O\Big({z_T^0}^3 / {q_T^0}^3\Big). \end{aligned}\right\} \tag{C 6}$$

Once inserted into (C 3), these approximations lead to

$$\left.\begin{aligned} l^{\text{HH}\,1}_{\;\;1} &= \frac{q_\rho^0}{q_T^0}\, T^0 + O\Big({z_T^0}^2 / {q_T^0}^2\Big), \\ l^{\text{HH}\,1}_{\;\;2} &= O\Big({z_T^0}^2 / {q_T^0}^2\Big), \\ l^{\text{HH}\,1}_{\;\;3} &= \rho^0, \end{aligned}\right\} \tag{C 7a}$$

$$\left.\begin{aligned} l^{\text{HH}\,2}_{\;\;1} &= T^0 \left[\sqrt{\left|1 - q_\rho^0/q_T^0\right|} + O\big(z_T^0/q_T^0\big)\right], \\ l^{\text{HH}\,2}_{\;\;2} &= \gamma\, M'^2\, z_T^0 \left[1 + O\big(z_T^0/q_T^0\big)\right], \\ l^{\text{HH}\,2}_{\;\;3} &= -\rho^0\, \frac{z_T^0}{q_T^0} = O\big(z_T^0/q_T^0\big), \end{aligned}\right\} \tag{C 7b}$$

$$\left.\begin{aligned} l^{\text{HH}\,3}_{\;\;1} &= T^0 \left[\sqrt{\left|1 - q_\rho^0/q_T^0\right|} + O\big(z_T^0/q_T^0\big)\right], \\ l^{\text{HH}\,3}_{\;\;2} &= \gamma\, M'^2\, z_T^0 \left[-1 + O\big(z_T^0/q_T^0\big)\right], \\ l^{\text{HH}\,3}_{\;\;3} &= \rho^0\, \frac{z_T^0}{q_T^0} = O\big(z_T^0/q_T^0\big), \end{aligned}\right\} \tag{C 7c}$$

respectively.

C.2. *Calculations specific to self-similar flows*

All of the above considerations as well as those of §§4.2.1, 4.2.2 are relevant to arbitrary one-dimensional non-viscous compressible flows with nonlinear heat conduction. When considering the self-similar flows of §3, the linear wave analysis of the time-dependent system (4.1) benefits from the following result: with the notation

$$\mathcal{T} = \mathrm{diag}\big(\bar{t}^{\alpha-1}\,,\ 1\,,\ \bar{t}^{1-\alpha}\big)\,,$$

system (4.1) is equivalent to

$$\frac{\partial \boldsymbol{U}^1}{\partial \bar{t}} + \bar{t}^{-1}\,\mathcal{T}^{-1}\left(\bar{t}^{2\alpha}\,\underline{\boldsymbol{A}}^0\,\frac{\partial^2 .}{\partial {m^0}^2} + \bar{t}^{\alpha}\,\underline{\boldsymbol{B}}^0\,\frac{\partial .}{\partial m^0} + \underline{\boldsymbol{C}}^0\right)\mathcal{T}\,\boldsymbol{U}^1 = \boldsymbol{0}, \tag{C 8}$$

where the matrices $\underline{\boldsymbol{A}}^0$, $\underline{\boldsymbol{B}}^0$, $\underline{\boldsymbol{C}}^0$ are functions of the sole reduced abscissa ξ. Accordingly, the properties of (4.1) may be inferred from those of these reduced matrices. In particular, the eigenvalues λ_k of $\boldsymbol{B}^0$ are such that

$$\lambda_k(m^0, \bar{t}) = \bar{t}^{\alpha-1}\,\Lambda_k(\xi), \quad k = 1, 2, 3,$$

where Λ_k are the eigenvalues of $\underline{\boldsymbol{B}}^0$, with corresponding left and right eigenvectors given by

$$\big(\bar{t}^{\alpha-1}\,L_1^k \quad L_2^k \quad \bar{t}^{1-\alpha}\,L_3^k\big)^{\top}, \quad \text{and} \quad \big(\bar{t}^{1-\alpha}\,R_1^k \quad R_2^k \quad \bar{t}^{\alpha-1}\,R_3^k\big)^{\top},$$

where $\boldsymbol{L}^k = (L_i^k)$ and $\boldsymbol{R}^k = (R_i^k)$ are, respectively, left and right eigenvectors of $\underline{\boldsymbol{B}}^0$ associated to the eigenvalue Λ_k. As a consequence, the linear-wave characteristic equations (4.9) can be written as

$$\bar{t}^{2\alpha-2}\,L_1^k\,\mathrm{d}\rho^1 + \bar{t}^{\alpha-1}\,L_2^k\,\mathrm{d}v_x^1 + L_3^k\,\mathrm{d}T^1 = 0, \quad \text{along } \mathcal{C}_k\text{:} \quad \frac{\mathrm{d}m^0}{\mathrm{d}\bar{t}} = \bar{t}^{\alpha-1}\,\Lambda_k, \quad k = 1, 2, 3,$$

inducing that the knowledge of the set of reduced functions $(\Lambda_k, \boldsymbol{L}^k)$, $k = 1, 2, 3$, is sufficient for assessing entirely the properties of (4.9).

REFERENCES

Boudesocque-Dubois, C., Gauthier, S. & Clarisse, J.-M. 2008 Self-similar solutions of unsteady ablation flows in inertial confinement fusion. *J. Fluid Mech.* **603**, 151–178.

Boudesocque-Dubois, C., Lombard, V., Gauthier, S. & Clarisse, J.-M. 2013 An adaptive multidomain Chebyshev method for nonlinear eigenvalue problems: Application to self-similar solutions of gas dynamics equations with nonlinear heat conduction. *J. Comput. Phys.* **235**, 723–741.

Bychkov, V., Modestov, M. & Law, C. K. 2015 Combustion phenomena in modern physics: I. Inertial confinement fusion. *Prog. Energy Combust. Sci.* **47**, 32–59.

Bychkov, V. V., Golberg, S. M. & Liberman, M. A. 1994 Self-consistent model of the Rayleigh–Taylor instability in ablatively accelerated laser plasma. *Phys. Plasmas* **1** (9), 2976–2986.

Clarisse, J.-M., Gauthier, S., Dastugue, L., Vallet, A. & Schneider, N. 2016 Transient effects in unstable ablation fronts and mixing layers in HEDP. *Phys. Scr.* **91**, 074005.

Clavin, P. & Masse, L. 2004 Instabilities of ablation fronts in inertial confinement fusion: A comparison with flames. *Phys. Plasmas* **11** (2), 690–705.

Goncharov, V. N., Betti, R., McCrory, R. L., Sorotokin, P. & Verdon, C. P. 1996 Self-consistent stability analysis of ablation fronts with large Froude numbers. *Phys. Plasmas* **3** (4), 1402–1414.

Goncharov, V. N., Skupsky, S., Boehly, T. R., Knauer, J. P., McKenty, P., Smalyuk, V. A., Town, R. P., Gotchev, O. V., Betti, R. & Meyerhofer, D. D. 2000 A model of laser imprinting. *Phys. Plasmas* **7** (5), 2062–2068.

Jacobson, N. 2009 *Basic algebra 1*, 2nd edn. Mineola, NY: Dover.

Kull, H. J. & Anisimov, S. I. 1986 Ablative stabilization in the incompressible Rayleigh–Taylor instability. *Phys. Fluids* **29**, 2067–2075.

Maxima 2010 Maxima, a computer algebra system. version 5.21.1. http://maxima.sourceforge.net/.

Nozaki, K. & Nishihara, K. 1980 Deflagration waves supported by thermal radiation. *J. Phys. Soc. Jpn.* **48** (3), 993–997.

Paolucci, S. 1982 On the filtering of sound from the Navier–Stokes equations. *Tech. Rep.* SAND-82-8257. Sandia National Laboratories.

Saillard, Y., Arnault, P. & Silvert, V. 2010 Principles of the radiative ablation modeling. *Phys. Plasmas* **17**, 123302.